Ultrafast relativistic electron probing of extreme magnetic fields

Brandon K. Russell,[1, a)] Paul T. Campbell,[1] Qian Qian,[1] Jason A. Cardarelli,[1] Stepan S. Bulanov,[2] Sergei V. Bulanov,[3, 4] Gabriele M. Grittani,[3] Daniel Seipt,[5] Louise Willingale,[1] and Alexander G. R. Thomas[1]

[1)] *Gérard Mourou Center for Ultrafast Optical Science, University of Michigan, 2200 Bonisteel Boulevard, Ann Arbor, Michigan 48109, USA*

[2)] *Lawrence Berkeley National Laboratory, Berkeley, California 94720, USA*

[3)] *ELI Beamlines Facility, The Extreme Light Infrastructure ERIC, Za Radnicí 835, Dolní Břežany, 25241, Czech Republic*

[4)] *National Institutes for Quantum and Radiological Science and Technology (QST), Kansai Photon Science Institute, Kyoto, 619-0215 Japan*

[5)] *Helmholtz Institute Jena, Fröbelstieg 3, 07743 Jena, Germany*

(Dated: 1 October 2023)

We investigate the suitability of using GeV laser wakefield accelerated electron beams to measure strong, $B > 0.1$ MT, magnetic fields. This method is explored as an alternative to proton deflectometry, which cannot be used for quantitative measurement using conventional analysis techniques at these extreme field strengths. Using such energetic electrons as a probe brings about several additional aspects for consideration, including beam divergence, detectors, and radiation reaction, which are considered here. Quantum radiation reaction on the probe is found to provide an additional measurement of the strength and length of fields, extending the standard deflectometry measurement that can only measure the path integrated fields. An experimental setup is proposed and measurement error is considered under near-term experimental conditions.

I. INTRODUCTION

Currently there is an international push to develop ultra-intense lasers ($I_L > 10^{23}$ W/cm^2)[1–5] motivated by the study of fundamental physics effects in ultra-strong electromagnetic fields and potential applications of high energy particle and photon sources generated by these fields[5–7]. These lasers may also be used to produce $B > 0.1$ MT (Giga-Gauss) strength magnetic fields during solid target interactions[8–11]. Such fields may allow for the study of magnetized processes expected in extreme astrophysical environments e.g., magnetic reconnection[12–14] and shock formation[15]. However, it is currently unclear how such strong fields can be measured in the laboratory.

Several methods for diagnosing the spatial and temporal dynamics of magnetic fields exist which can generally be placed into two categories: optical methods and particle methods. Optical methods typically use a diagnostic laser to probe the plasma, and magnetic field information is encoded into the polarization of the laser through the Faraday effect[16,17]. Other experiments have used plasma wave cutoff frequencies to estimate the range of field strengths[18]. These methods suffer from an inability to probe plasmas with densities greater than the critical density for the diagnostic laser and struggle to probe plasmas produced from solid targets due to the steep density gradients near the target surface. The critical density is given by, $n_{crit} = m_e\varepsilon_0\omega_L^2/e^2$, where ω_L is the frequency of the probing laser. Most experiments will use a higher-order harmonic of the driving pulse to probe the plasma such that it can probe further into the dense plasma which would otherwise be inaccessible for the fundamental. Even with higher-order harmonics, at the standard wavelength of most high-power laser facilities (~ 1 μm) the fields generated in laser-solid interactions cannot be probed. Faraday rotation using x-rays has been proposed as a solution, but requires a source of well characterized x-rays co-located with a high-intensity laser facility[10].

Particle methods have involved the use of protons or electrons to probe the electric and magnetic fields in high energy density (HED) plasmas. In typical HED experiments, a secondary laser pulse accelerates a beam of protons[19] or electrons[20–24]. Electrons accelerated by conventional linear accelerators have also been demonstrated as a probe[25,26]. As the beam passes through the plasma, the particle trajectories are altered by the electric and magnetic fields. Typically, the thickness of plasma and fields traversed by the particles are small and the spatial profile of the beam is not significantly modified at the exit of the plamsa. It is only after propagating away from the plasma that changes in particle transverse momen-tum accumulated in the plasma manifest in a modulated beam spatial profile. This modulated profile is measured by stacks of film or scintillating screens. A recent par-ticle method has also been proposed to measure strong magnetic fields using the spin of electrons[27] that interact with the target magnetic fields, however it is unclear how spin-polarization can be measured to the required accuracy. Additionally, this technique is only applicable to measurements of fields near the laser focal spot, not to get a global picture as would be needed in magnetized experiments, e.g. laser-driven magnetic reconnection[28,29].

Many experiments have relied on proton deflectometry[30] to measure and identify HED electromagnetic phenomena such as laser-driven magnetic field generation[31–34], Weibel-type filamentation and magnetic

[a)] Electronic mail: bkruss@umich.edu

self-organization[35,36], high power laser channeling[37], and laboratory magnetic reconnection[28,38–41]. One approach for producing energetic protons involves using many laser beams to implode a capsule containing D-^{3}He fuel. Fusion of the fuel results in a quasi-monoenergetic, quasi-isotropic source of 3 and 14.7 MeV protons. These protons can then be captured on a piece of CR-39. A second method for producing energetic protons is through the the Target Normal Sheath Acceleration (TNSA) mechanism where a high intensity laser pulse interacts with a solid-target, accelerating a proton beam to multi-MeV energies[42–47]. The broad spectrum of accelerated proton energies leads to a temporal dispersion during transit from the source to the main interaction, with higher energy protons arriving earlier than lower energies. The Bragg peak behavior of ion stopping means that each energy penetrates to a unique depth in the detector. Therefore, a stack of radiochromic film can capture a time series of images of the electromagnetic field dynamics in a single shot[19,48].

Images generated from proton deflectometry are often used as a qualitative diagnostic. Features in the image are compared to simulation or simple models and synthetic proton images. However, quantitative measurements of path integrated electric and magnetic fields can be extracted from the relative deflections of protons in the image[49–51]. One of the main assumptions made in proton deflectometry analysis techniques is that the deflection angle due to fields is small compared to the initial angular spread of the protons passing through the fields, and the trajectories of deflected protons do not cross. For the protons used in typical TNSA deflectometry, energies are on the order of 10 MeV. At these energies, deflection angles in the 10 kT magnetic fields seen in relativistic laser-plasma interactions are too large to allow for quantitative measurements of the magnetic fields using standard analysis methods.

Electrons accelerated by laser-wakefield acceleration (LWFA) may be a solution to probing these fields and even the more extreme 0.1 MT fields expected from next generation lasers. The mechanisms for accelerating electrons are significantly more efficient than those for ions. This has allowed for electrons to reach energies of ~ 8 GeV[52] compared to peak energies $100 - 150$ MeV for protons[53,54]. Although, the acceleration of much higher energy protons may be possible through novel acceleration mechanisms[55]. Even GeV electron beams which are routinely produced will experience smaller deflection angles than a 100 MeV proton, therefore they should be able to measure stronger magnetic fields.

In this paper, we will evaluate LWFA electrons as a potential probe for measuring strong magnetic fields. In section II we will review the equations used in the current deflectometry analysis and describe the limits of this technique. Section III will evaluate the major considerations that must be made when using LWFA electrons including divergence, detectors, and radiation reaction on the probe beam which may be important to imaging with GeV energy beams. Section IV will incorporate the ideas of section III to propose a realistic experimental setup using LWFA electrons to probe the strong magnetic fields produced during ultra-intense laser-solid interactions.

II. REVIEW OF THEORY OF DEFLECTOMETRY ANALYSIS

Charged particle deflectometry experiments generally operate in a point-projection geometry. A schematic of a typical experiment is shown in Fig. 1. A source of particles, whether a broadband proton source accelerated via the TNSA mechanism, a monoenergetic proton source generated by D-^{3}He fusion or from a novel acceleration method[56–58], or a laser-wakefield electron accelerator, is located a distance l from the main interaction at the object plane. The detector, often a stack of radiochromic film (RCF), a piece of CR-39, or scintillating screen (in the case of electrons), is positioned a distance L behind the main interaction. In most experiments, $L \gg l$ and $l \gg a$, where a is the characteristic spatial scale of the field structure being diagnosed. However, recent experiments using LWFA electrons have operated in the opposite limit $L \ll l$[23]. This method was used to measure the fields formed in laser-wakefield channels. Such a geometry could be used for the measurement of magnetic fields, however for extremely strong fields the scintillating screen would need to be placed very close to the object plane. In addition to the practical challenge of placing a screen in such close proximity to a solid target, high intensity laser-solid interactions tend to produce large fluxes of high energy ions and x-ray radiation which would result in significant background signal. Moving the detector further away can greatly improve the signal-to-noise due to the beam-like nature of the LWFA electron probe compared to large divergence emission from laser-solid interactions. A potential solution to the detector position problem has recently been demonstrated. The detector can be placed further from the interaction by using beam optics to relay image the electron beam, allowing the $L \ll l$ limit to be maintained. However, this solution adds significant complexity due to the addition of beam optics[26,59]. Therefore, from this point on we will only consider the $L \gg l$ geometry.

In the work by Kugland *et al.*[49], it was shown that for a point source one can relate the intensity at a position (x_0, y_0) in the object plane to the intensity at a position (x, y) in the image plane by calculating the transformation of each infinitesimally small area $dx_0 dy_0$ to the corresponding area $dxdy$. We can find this transformation by first noting that a particle which passes through the point (x_0,y_0) will experience some deflections due to the fields α_x, α_y, and will have an initial angle x_0/l, y_0/l if it starts from a point source. The equations for the position in the image plane are then,

$$x = x_0 + \frac{x_0}{l}L + \alpha_x L, \tag{1}$$

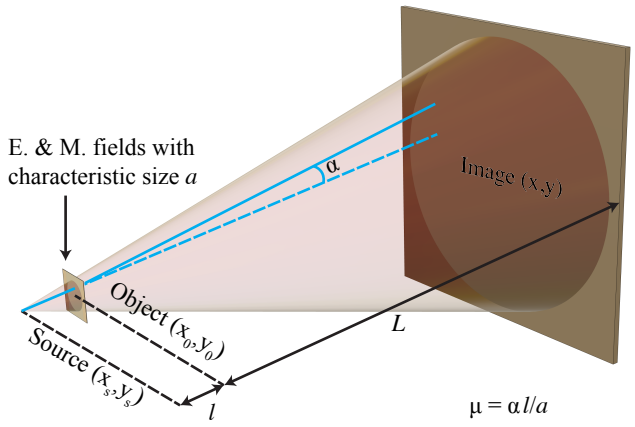

FIG. 1: Schematic representation of a typical point-projection proton radiography experiment.

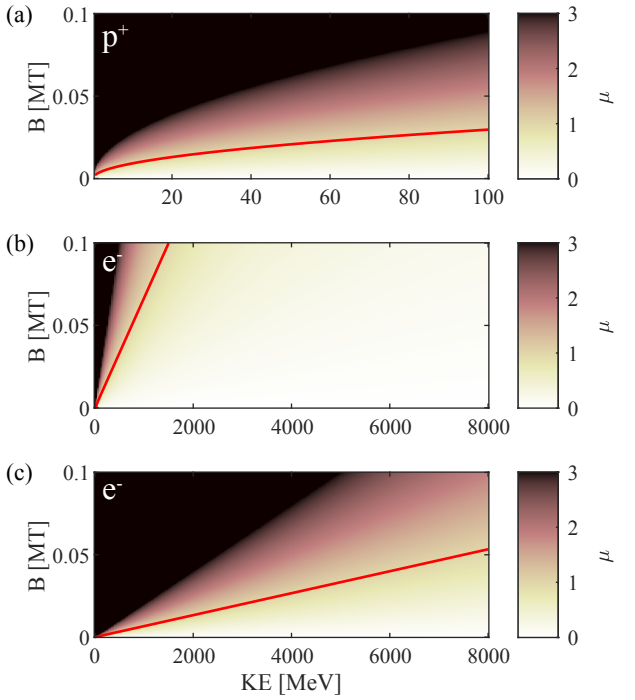

FIG. 2: Comparison of deflectometry nonlinearity parameter μ for (a) protons with $l = 5$ mm, $a = 100$ μm, field thickness $l_B = 1$ μm (b) electrons using this same geometry (c) electrons with $l = 5$ cm. Red curves show where $\mu = 1$.

$$y = y_0 + \frac{y_0}{l}L + \alpha_y L. \tag{2}$$

This can be viewed as a coordinate transformation, therefore we can write,

$$\begin{bmatrix} dx \\ dy \end{bmatrix} = \begin{bmatrix} 1 + \frac{L}{l} + \frac{\partial \alpha_x}{\partial x_0}L & \frac{\partial \alpha_x}{\partial y_0}L \\ \frac{\partial \alpha_y}{\partial x_0}L & 1 + \frac{L}{l} + \frac{\partial \alpha_y}{\partial y_0}L \end{bmatrix} \begin{bmatrix} dx_0 \\ dy_0 \end{bmatrix}, \tag{3}$$

where the determinant of the transformation matrix $|\partial(x,y)/\partial(x_0,y_0)|$ is equal to the change in area due to the coordinate transformation. The mapping between the undisturbed proton beam distribution, $I_0(x_0, y_0)$ and the deflected distribution $I(x, y)$ at the image plane is then determined by,

$$I(x,y) = \frac{I_0(x_0,y_0)}{|\frac{\partial(x,y)}{\partial(x_0,y_0)}|}. \tag{4}$$

Assuming small deflections for a particle traveling with a constant velocity v_z in the $\hat{z}$ direction the deflections are related to the electric or magnetic fields in the plasma by,

$$\alpha_x = \frac{\Delta p_x}{p_z} = -\frac{q}{\gamma m v_z}\int_{-\infty}^{\infty} B_y dz + \frac{q}{\gamma m v_z^2}\int_{-\infty}^{\infty} E_x dz, \tag{5}$$

$$\alpha_y = \frac{\Delta p_y}{p_z} = \frac{q}{\gamma m v_z}\int_{-\infty}^{\infty} B_x dz + \frac{q}{\gamma m v_z^2}\int_{-\infty}^{\infty} E_y dz. \tag{6}$$

As α increases, the relationships between the image and object coordinates become nonlinear, and for very large α, particle trajectories can begin to cross and form strong caustics in the image. In the caustic, the relationship between I and I_0 is no longer unique, significantly limiting the quantitative field information that can extracted from the images. The following dimensionless parameter characterizes the nonlinearity of the mapping[49],

$$\mu \equiv \alpha l/a\,. \tag{7}$$

When $\mu \ll 1$, then the mapping is approximately linear and caustics can form when $\mu > 1$.

The theory reviewed in this section was derived under the assumption of a point source. However, real particle sources have finite source sizes that will result in blur-ring of the image. This complication was considered by Kugland *et al.* through the following simple argument. A source can be viewed as a superposition of multiple point sources with varying magnitudes depending on the particle distribution function. A source placed at a distance a_s from the original point source perpendicular to the probing direction will generate an image displaced from the original point source by a distance $a_s L/l$. If $L \gg l$ then the fields with a characteristic size a will generate an image with size aL/l. The source must then have a characteristic size $a_s \ll a$ to resolve the fields. For TNSA protons and LWFA electrons, source sizes are $\mathcal{O}(\mu\text{m})$ while characteristic magnetic field sizes in laser-solid interactions $\mathcal{O}(100\ \mu\text{m})$, therefore the fields can be resolved by these particle sources.

III. SOME MAJOR CONSIDERATIONS

As was noted in the introduction, even for current relativistic laser intensities, magnetic field strengths in solid target interactions are too strong to be measured quantitatively by protons. To show this, μ has been plotted in

Fig. 2(a) using a realistic proton probing geometry with a source to object plane distance $l = 5$ mm. The magnetic fields are taken to have a thickness $l_B = 1$ μm and a characteristic size of $a = 100$ μm. A red line showing $\mu = 1$ has been plotted to show where the imaging nonlinearity becomes too large to perform quantitative analysis. Even for the highest proton energies that might be expected from TNSA on facilities like OMEGA EP, perhaps 50 MeV, the maximum measurable strengths are < 20 kT. Although protons experience smaller deflections than electrons at the same energy due to their larger mass, electrons can be accelerated to higher energies, therefore in the same geometry much stronger fields can be measured (Fig. 2(b)). Note the difference in the scaling of the $\mu = 1$ line differs for the highly relativistic electrons and the nonrelativistic protons. From Eqns. (5) and (6), if the particle is highly relativistic, $v_z \approx c$ then $\alpha \propto 1/\gamma$. The particle kinetic energy is approximately proportional to γ, therefore as the kinetic energy increases, the path integrated field must increase proportionally to keep μ constant, giving a linear $\mu = 1$ curve. This is not the case for protons where the $\mu = 1$ curve is nonlinear due to the $1/v_z$ scaling in α for these energies.

There are many differences in proton and electron probing that are not captured in this simple comparison. In the following sections, some of the major additional considerations of electrons probing will be discussed. Many of these considerations will be true even for measuring weak fields, however there will be a emphasis on the measurement of strong fields.

A. Divergence Angle

The main issue with the comparison shown in Fig. 2 is the characteristic beam divergence angle. TNSA proton beams typically have large divergence angles of ~ 0.7 rad full angle and protons generated from capsule implosions move out in 4π steradians. Considering the characteristic scale of the azimuthal fields generated in solid target laser interactions is $\mathcal{O}(100$ μm), the geometry used in Fig. 2(a) is realistic to obtain a complete picture of the fields. However, the divergence angle of electrons from LWFA is much smaller $\mathcal{O}$(mrad). Therefore, the source-to-object-plane distance must be several centimeters to obtain a picture of the complete fields. As shown in Fig. 2(c), this will greatly change μ, and the maximum field strength that can be measured is greatly reduced and more comparable to protons.

A potential solution to this problem is to use beam optics to strongly focus the beam millimeters before the object plane to increase the divergence. However, focusing a relativistic electron beam with an energy spread using quadrupoles is challenging. A pair or triplet of quadrupoles is required to symmetrically focus a beam, however this only works for a narrow range of energies. Particles with other energies will be focused to different focal planes with different path lengths, causing blurring in the deflected image. Even without this complication, with the current magnetic field gradients that quadrupoles can provide (~ 500 T/m), it is possible that focusing is not sufficient to increase the divergence of the beam enough to allow for quantitative measurements of the magnetic fields of interest in this work.

To investigate this, consider for simplicity a collimated electron beam being focused by a single optical element. For a quadrupole the beam will be focused along one axis and defocused along the other. The transverse position of a ray of a beam that propagates through the position (x_i, y_i) at the entrance of the quadrupole will be focused along one axis as[60],

$$y(y_i, L_m) = y_i \cos(\sqrt{k} L_m), \tag{8}$$

and defocused along the other as,

$$x(x_i, L_m) = x_i \cosh(\sqrt{k} L_m). \tag{9}$$

Here, L_m is the length of the quadrupole that the beam has propagated through, and

$$k = \frac{e}{\gamma m c} \frac{\partial B}{\partial r}, \tag{10}$$

defines the strength of the quadrupole for a particular particle energy. Note that the focusing is periodic, while the defocused position is unbounded. If the quadrupole is too long, the beam will collide with the inner wall of the quadrupole. This sets a maximum angle that a beam can have after propagating through a particular quadrupole. The exit angle of the beam in the two directions is given by,

$$y'(y_i, L_m) = -y_i \sqrt{k} \sin(\sqrt{k} L_m), \tag{11}$$

$$x'(x_i, L_m) = x_i \sqrt{k} \sinh(\sqrt{k} L_m). \tag{12}$$

Setting x equal to r_m, the radius of the quadrupole aperture, and solving for $\sqrt{k} L_m$ gives the maximum length before the defocusing beam collides with the quadrupole structure. Substituting this into Eqn. (12), results in:

$$x'(x_i) = \sqrt{k(r_m^2 - x_i^2)}. \tag{13}$$

The maximum angle from defocusing appears in the limit of small x_i, where $x' \approx r_m \sqrt{k}$. In the focusing (y-direction) the maximum angle occurs when $\sqrt{k} L_m = \pi/2$. This maximum angle is $y_i \sqrt{k}$ and occurs when $y = 0$. Note that the maximum y_i is the inner radius of the quadrupole r_m, therefore the maximum $x'_{max} = y'_{max} = r_m \sqrt{k}$. However these angles appear under different conditions, specifically $x_i \to 0$ and $y_i = r_m$. Taking x_i and y_i to be the initial transverse extent of the beam along the two axes, note that they cannot be controlled independently and will be defined by the beam as it exits the wakefield. Such a beam will likely have $x_i \approx y_i$,

therefore a maximum angle in the focusing direction of $r_m\sqrt{k}$ cannot be achieved because the beam would immediately collide with the quadrupole along the defocusing axis. This angle can almost be obtained in the defocusing direction, however it would greatly limit the angle in the focusing direction.

Now consider how this angle can be used to determine the maximum measurable magnetic field. First note that μ is a ratio of angles. The scattering angle α is compared to the angle formed by a diverging beam that probes a region of size a placed a distance l from the beam source. We can similarly write, $\mu = \alpha/x'$. The minimum x' required to achieve a $\mu < 1$ can then be solved for. Assuming that the beam is relativistic, $\alpha \approx e\mathcal{B}/\gamma mc$, where $\mathcal{B} = \int_{-\infty}^{\infty} B_\perp dz_0$ is the path integrated perpendicular magnetic field. Substituting this into the $\mu < 1$ inequality gives,

$$\mathcal{B} < r_m\sqrt{\frac{\gamma mc\partial B/\partial r}{e}}. \tag{14}$$

Taking realistic parameters for a quadrupole of $r_m = 2.5$ mm, $\partial B/\partial r = 500$ T/m, $\gamma = 1955$ (1 GeV), then $\mathcal{B} \approx 0.1$ Tm. This is similar to the $\mathcal{B} > 0.1$ Tm fields expected from laser solid interactions ($B > 0.1$ MT, $l_B > 1$ μm)[11]. However, the focusing is again not symmetric, therefore this is only true for one of the axes. A better optic for this problem may be a plasma lens because it focuses symmetrically[61]. While the field gradients are stronger $\partial B/\partial r \approx 3000$ T/m, the smaller acceptance radius $r_m = 0.125$ mm limits the measurement to even weaker 0.0125 Tm path integrated fields. Larger and stronger plasma lenses will need to be produced before they become a viable solution to the divergence problem.

B. Detectors

The way protons deposit energy in materials is very different from electrons, therefore the detectors that can be used for protons do not work for electrons. One of the main benefits of using protons is that due to their Bragg peak they can be detected on stacks of radiochromic film where each piece of film in the stack detects a small range of proton energies. For TNSA proton beams where the beam energy spread is large, due to time of flight differences, a single stack of radiochromic film can obtain a timeseries of data. Additionally, by only measuring a small range of energies any effects due to having an energy spread are negligible. However, such a detector does not exist for electrons as they do not have a Bragg peak. In an experiment, electrons which will likely be detected by LANEX[62], a material that scintillates when electrons are incident on it. For this type of detector all electron signal will be integrated. Deflection angle in the object plane varies with particle energy, therefore features will be blurred due to the beam energy spread.

If the electrons have a Gaussian energy distribution and propagate to the object plane from a point source, electrons passing through the point x_0 in the object plane will be deflected such that the maximum of the distribution is found in the image plane at the position:

$$x_{max} = \frac{ecL\mathcal{B}}{E_0} + Mx_0. \tag{15}$$

Here $\mathcal{B} = \int_{-\infty}^{\infty} B_y(x_0)\, dz_0$, $M = (l + L)/l$ is the magnification and E_0 is the mean energy of the distribution.

Given an energy spread σ_e for the distribution, the full-width half-maximum (FWHM) of the beam in the image plane will be:

$$\Delta x_{energy} = ecL\mathcal{B}\frac{2\sqrt{2\ln(2)\sigma_E^2}}{E_0^2 - 2\ln(2)\sigma_E^2}. \tag{16}$$

Similar to the Rayleigh resolution criterion we can note that only features with sizes greater than Δx_{energy} in the image plane will be resolved. Fig. 3 demonstrates how this energy spread appears in the image plane. See Appendix A for the derivation of these equations.

From Eqn. (16), if E_0, σ_E, and the probing geometry are known and Δx_{energy} can be measured, then the path integrated B-field can be calculated. If a beam with a very narrow energy spread is used to probe a small region of the object plane, then based on the spatial spread in the image plane, the field at that point can be estimated. The path integrated magnetic fields can similarly be calculated using Eqn. (15) by measuring the position where the peak of the distribution is deflected. This idea will be revisited in section IV.

C. QED Considerations

As the high energy electrons of the probe beam are deflected by the strong fields in the object plane they will radiate. By emitting photons, the electron beam gives up energy thereby shifting the mean energy of the beam and causing the energy spread of the beam to increase. These effects are given by the equations[63],

$$\left(\frac{d\langle\mathbf{p}\rangle}{dt}\right)_{mod\ cl} = -\frac{\langle gP_{cl}\hat{\mathbf{p}}\rangle}{c}, \tag{17}$$

$$\left(\frac{d\sigma^2}{dt}\right)_{st} \approx \frac{\alpha_f cb^2}{\lambda_c}\left(\frac{55b}{24\sqrt{3}}\langle\gamma\rangle^4 - \frac{8}{3}\sigma^2\langle\gamma\rangle\right) \tag{18}$$

where Eqn. (17) gives the change in average value of the momentum and Eqn. (18) gives the change in the variance of a beam with $\sigma^2 = \langle\gamma^2\rangle - \langle\gamma\rangle^2$. Eqn. (18) is only valid assuming the beam energy distribution is always Gaussian, the energy spread is small $\sigma \ll \langle\gamma\rangle$ and $\eta \ll 1$. P_{cl} is the power classically emitted to synchrotron radiation given by,

$$P_{cl} = \frac{2\alpha_f}{3\lambda_c}m_e c^3\eta^2, \tag{19}$$

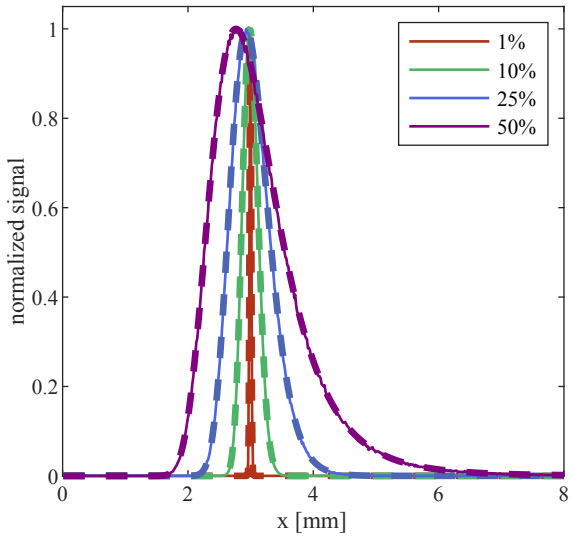

FIG. 3: Spread in image plane of an electron beam calculated from a particle tracking code assuming deflections in a single plane (solid lines) and Eqn. (A4) from Appendix A (dashed lines). The following parameters were used: $E_0 = 1$ GeV, $l = 1$ cm, $L = 1$ m, $\mathcal{B} = 0.01$ Tm, σ_E varied to generate a FWHM energy spread as shown in the legend.

where α_f is the fine structure constant, $\lambda\!\!\!^{-}_c$ is the reduced Compton wavelength, and η is the quantum efficiency parameter defined as the ratio of the field strength in the rest frame of the electron beam to the Schwinger field $E_s = 1.32 \times 10^{18}$ Vm^{-1}. For a highly relativistic beam where $\gamma \gg 1$, $\eta \equiv \gamma b = \gamma|\mathbf{E}_\perp + \mathbf{v} \times \mathbf{B}|/E_s$. The Gaunt factor $g(\eta)$ acts as a quantum correction to the classical emission spectrum for η approaching unity and has been fit to $g(\eta) \approx [1 + 4.8(1+\eta)\ln(1+1.7\eta) + 2.44\eta^2]^{-2/3}$.

Consider an electron beam with a Gaussian energy spread propagating through a constant magnetic field that is perpendicular to the propagation direction. We can solve analytically for the decay in the average value of the Lorentz factor γ using Eqn. (17),

$$\langle\gamma\rangle \approx \left(\frac{1}{\langle\gamma_0\rangle} + \kappa t\right)^{-1}, \tag{20}$$

$$\kappa = \frac{2\alpha_f c^3 B_\perp^2}{3\lambda\!\!\!^{-}_c E_s^2}, \tag{21}$$

where $\langle\gamma_0\rangle$ is the average initial Lorentz factor. Additionally we have taken $\langle p\rangle \approx m_e c\langle\gamma\rangle$. Here we have assumed $\eta \ll 1$ so $g \approx 1$, and additionally $\sigma \ll \langle\gamma\rangle$. This can be rearranged to solve for the perpendicular magnetic field,

$$B_\perp = \sqrt{\frac{3\lambda\!\!\!^{-}_c E_s^2}{2\alpha_f c^2 l_B}\left(\frac{1}{\langle\gamma\rangle} - \frac{1}{\langle\gamma_0\rangle}\right)}, \tag{22}$$

where $l_B = ct$ is the length of the magnetic field assuming highly relativistic electrons. Eqn. (20) can be substituted into Eqn. (18) to give,

$$\sigma = \langle\gamma\rangle^2\sqrt{\frac{\sigma_0^2}{\langle\gamma_0\rangle^4} + At}, \tag{23}$$

where $A = \alpha_f c^4 B_\perp^3 55/24 E_s^3 \sqrt{3}\lambda\!\!\!^{-}_c$. See Appendix B for the derivation of this equation. We can note an interesting result here. If the initial and final mean γ and energy spread can be measured then Eqn. (20) will give $B_\perp^2 l_B$ while Eqn. (23) will give $B_\perp^3 l_B$. Additionally, if the deflection of the beam is measured, the solution will give $B_\perp l_B$, therefore if at least two of the three measurements can be made then $B_\perp$ and l_B can be found uniquely.

If η is not $\ll 1$, then $g \neq 1$ and cannot be removed from the integrals solved to get Eqns. (20) and (23). An analytical solution can be found by Taylor expanding g, however it is not simple to manipulate the solutions to obtain $B_\perp$. If necessary, the best option may be to numerically solve Eqn. (17) and the version of Eqn. (18) without the $\eta \ll 1$ approximation (Eqn. (3.4) reported by Ridgers *et al.*[63]).

The range of validity of the approximations used to derive these analytical expressions can be found by comparing to simulated results. Fig. 4 shows a comparison of the analytical model (Eqn. (20)) to simulated results. The simulations were performed using the particle-in-cell (PIC) code OSIRIS[64,65]. In the code, a Monte Carlo algorithm is coupled to the classical PIC loop to enable the simulation of multi-photon Compton scatting and multi-photon Breit-Wheeler pair creation under the local constant field approximation (LCFA). The simulations start with a collimated, 1 GeV mono-energetic electron beam. The beam is then propagated through a 2D region of constant magnetic field directed perpendicular to the electron motion. Simulations were performed for a range of magnetic field strengths varying from 0.01 to 1 MT, and the length of the constant field region from 0.01 to 10 μm. This parameter space is motivated by the range of values we might expect based on simulations of laser-solid interactions[11]. The results from the PIC simulation are taken to be the reference or "ground truth" value. Fig. 4 shows the relative difference of the mean energy loss between the PIC simulation results and the analytic model ($|\langle E\rangle_{PIC} - \langle E\rangle_{analytic}|/\langle E\rangle_{PIC}$) using Eqn. (20).

For the parameter range shown here, the analytic model well predicts the mean energy loss when the magnetic field strength is below 0.05 MT. The prediction assumes $\eta \ll 1$, therefore it cannot give an accurate prediction at large field strengths. The nonlinearity η ranges from 0.0044 to 0.44 for the simulated values. Similar results are found for the analytical expression for the energy spread (Eqn. (23)). Additionally, note that the LCFA used for the simulations will be invalid when the magnetic fields are weak and short because the photon formation length, $l_{formation} = m_e c/eB$ will exceed the length of the fields. This region has been blocked out

in Fig. 4. A similar comparison was performed for the numerical integration of Eqns. (17) and (18). A better agreement with the PIC simulations in mean energy and energy spread was found from these equations. However, when the magnetic field strength exceeds 0.5 MT ($\eta > 0.22$), the numerical integration cannot precisely predict the energy spread. This is because Eqn. (18) assumes the shape of energy distribution to be approximately Gaussian. However, when quantum radiation reaction is significant, the energy distribution deviates from the Gaussian distribution.

Given the exact measurement of the initial and final energy and energy spread of the electron beam, Eqns. (22) and (23) correspond to two lines of solutions for possible $B_\perp$ and l_B. These lines only cross at a single point giving a unique solution for these parameters. In Fig. 5, Eqns. (17) and (18) were solved numerically to find the mean energy and energy spread after passing through a range of field strengths and lengths of field. The colormap shows the energy spread σ_E normalized to the average energy of the beam $\langle E \rangle$. The beam is initially 1 GeV and monoenergetic. The cyan line is a line of constant final mean energy and the blue line is a line of constant energy spread. The values for final mean energy and energy spread were chosen such that they would result in a crossing point at 0.2 MT, 2 μm. An OSIRIS simulation was run to confirm that a 0.2 MT, 2 μm constant magnetic field would result in the expected mean energy and energy spread and is plotted as a white star. The calculated strength and length of field from Eqns. (22) and (23) are plotted as a black star, which underestimates the strength, and overestimates the length of the field. This is due to the assumption of small η being invalid for the simulated parameters. Although the analytical equations do not precisely predict the crossing point, they allow for an order-of-magnitude estimation of the strength and length of fields.

For an experiment, similar analysis could be performed, where all solutions that would result in the measured final mean energy and energy spread given a measured initial energy and energy spread could be solved for numerically. However, experimental measurements have errors. Error in the measurement of energy spread and mean energy will result in the lines in Fig. 5 having finite widths. These widths will result in a crescent-shaped region of overlap, i.e. error in the strength and length of field. The aspect ratio ($\Delta B_\perp / \Delta l_B$) of this region of overlap will depend non-linearly on the position of overlap of the lines. This effect is demonstrated in Fig. 6, in which a 10% measurement error in mean energy loss and spread is assumed. Taking the measured mean energy loss to be 51 MeV ($\Delta\langle\gamma\rangle = 100$), the red, blue, and purple regions show the possible values of B-field strength and length if the energy spread is 10%, 8%, or 6% respectively. If the lines cross at large B and small l_B, then there will be a much larger error in B than l_B. If they cross at small B and large l_B, there will be a much larger error in l_B than B. In section IV the way these errors may appear in an experiment using realistic detectors is discussed.

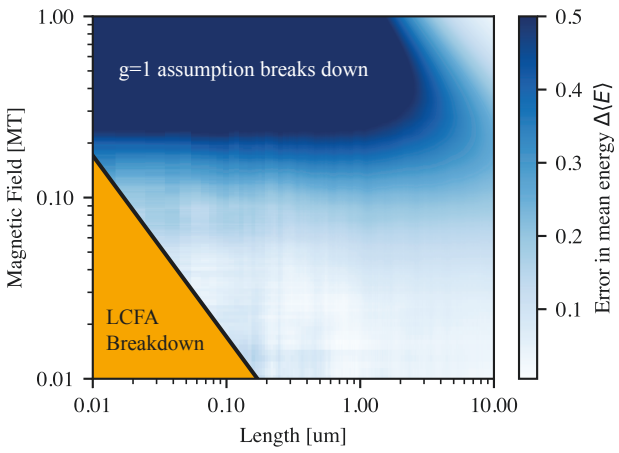

FIG. 4: Relative difference of the mean energy prediction between the PIC simulations and simplified analytic model. The orange region marks the parameter space where the LCFA breaks down. The dark blue region shows where the simplified analytic model breaks down.

D. Front and back surface magnetic fields

The arguments we have made so far are valid for magnetic fields that are uni-directional. The magnetic fields produced in high intensity laser interactions with thin foils are indeed not uni-directional. Azimuthal fields form on the front and back surface of the target with opposite polarity. This has been shown in images formed by proton deflectometry where the front and back surface fields will focus and defocus the probing protons creating multiple features in the deflected image[34]. To solve for the strength of the fields, the shape of the fields must be assumed and the strength and length of the fields must be scanned until these features are approximately reproduced.

If we consider a very small, narrow divergence electron beam with a Gaussian energy spread probing a region of the front surface fields it will be deflected and particles of different energies will have different deflection angles as described in section III B. Neglecting scattering in the target, the electron will freely propagate, translating the position of the electrons by $\Delta x_0(E)$ in the object plane. At the rear surface of the target these electrons will again be deflected, but in the opposite direction and perhaps by a different amount depending on the ratio of the front to back surface path integrated magnetic fields that each electron experiences. This will result in an overall reduction in the deflection angle of the particles because the deflection angle depends on the sign of the

fields. The position in the image plane is given by:

$$x = x_0 + \left(\frac{x_0}{l} + \alpha_{x,f}(x_0, E)\right)(d+L) + \alpha_{x,b}(x_0 + \Delta x_0, E)L, \tag{24}$$

where d is the thickness of the target, and the subscripts f and b, refer to the front and back of the target. In the thin target limit where $d \to 0$, $\Delta x_0 \to 0$ and the equation simplifies to:

$$x = x_0 + \frac{x_0}{l}L + (\alpha_{x,f}(x_0, E) + \alpha_{x,b}(x_0, E))L. \tag{25}$$

Considering deflections only due to constant perpendicular (y-directed) magnetic fields, this simply results in an additional term in the path integral of the magnetic field $\mathcal{B} = \int_{-\infty}^{\infty} B_y dz = B_{y,f} l_{B,f} + B_{y,b} l_{B,b}$. From Eqn. (15), by knowing the position of the maximum in the image plane we can calculate the complete path integrated magnetic fields that the electrons propagated through. The rear surface fields will have the opposite sign of the front surface fields, therefore x_{max} will be smaller than expected from the front surface fields alone. In addition to the thin target approximation, here we have additionally neglected radiation reaction which will cause particles to have lower energies when interacting with the rear surface fields thereby increasing the deflection by the rear surface fields. This approximation is valid given that particles do not lose a significant amount of energy in the front surface fields.

Now consider the effects of radiation reaction on the beam as it propagates through the fields. Unlike the deflection which depends on the sign of the fields, radiation reaction only depends on the angle of the fields with respect to the propagation direction of the electrons through the quantum non-linearity parameter η. After passing through the front surface magnetic fields the mean energy of the electron beam will change as described by Eqn. (20). After passing through the back surface fields the mean energy of the beam will be further reduced, however this effect is non-linear. It is described by:

$$\langle\gamma\rangle \approx \left(\frac{1}{\langle\gamma_0\rangle} + \kappa_f t_f + \kappa_b t_b\right)^{-1}, \tag{26}$$

where κ_f and κ_b are the front and back surface κ which just differ by the strength of the magnetic field. The time of propagation through the fields t_f and t_b can again be taken as the length of the fields $l_{B,f}$ and $l_{B,b}$ divided by the speed of light for highly relativistic beams. Similarly, the energy spread after passing through front and back surface fields can be obtained:

$$\sigma = \langle\gamma\rangle^2 \sqrt{\frac{\sigma_0^2}{\langle\gamma_0\rangle^4} + A_f t_f + A_b t_b}, \tag{27}$$

where $\langle\gamma\rangle$ is from Eqn. (26).

The addition of the rear surface fields adds significant complexity to finding the strength and length of the fields. From the shift in mean energy of the beam alone we can extract $B_{\perp,f}^2 l_{B,f} + B_{\perp,b}^2 l_{B,b}$. With the energy spread due to radiation reaction $B_{\perp,f}^3 l_{B,f} + B_{\perp,b}^3 l_{B,b}$ can be obtained. From the deflection in the thin target limit, neglecting radiation effects, $B_{\perp,f} l_{B,f} + B_{\perp,b} l_{B,b}$ can be calculated. From these measurements alone all parameters $(B_{\perp,f}, B_{\perp,b}, l_{B,f}, l_{B,b})$ cannot be obtained, and additional equations must be found or assumptions must be used to constrain the solutions. This statement is true for the simplified equations we have derived here. However, it is possible that additional information could be found though equations with fewer approximations. For example, by taking the target to be thin, the deflection angle only depends on the path integrated field. However, if the target is thick the beam position will shift between the front and back surface fields. This shift will result in a different deflected position depending on the order that the fields are probed, i.e. front then back or back then front. Probing from two directions may therefore provide the additional information necessary to calculate the four unknown values for the fields. It is also possible that a method exists that could inhibit the generation of back surface fields or to have the back surface fields be short-lived such that the dominant fields being probe are the front surface fields. Varying the front and rear surface pre-plasma scale length may allow for such an ef-fect. In general, the information from both energy loss and deflection may help constrain measurement of the magnetic fields.

IV. PROPOSED EXPERIMENTAL SETUP

In the previous sections we showed that electron probing cannot be performed in a similar way to how proton deflectometry is currently done, due to the small divergence angle of the beams. Even for GeV beams, obtaining a spatially resolved measurement of the $\mathcal{O}(0.1$ MT) magnetic fields using the standard deflectometry inversion technique[49] may not be possible. Instead, here we propose an experimental setup to uniquely measure the length and strength of the magnetic fields leveraging quantum radiation reaction using the ideas discussed in the previous section.

A. Description of setup

Fig. 7 shows the setup for the measurement of the strong (> 0.1 MT) azimuthal magnetic fields generated by an ultra-intense ($I \sim 10^{23}\,\mathrm{W/cm^2}$) laser interacting with a few micron thick foil. As previously mentioned, this is an important set of fields to consider because these fields may be used in future studies of magnetized pro-cesses, e.g. magnetic reconnection[28,41,66]. This setup be-gins with a gas jet or gas cell into which a short (10's of fs) laser pulse is focused using a high f-number fo-cusing optic. The high energy GeV beams necessary for

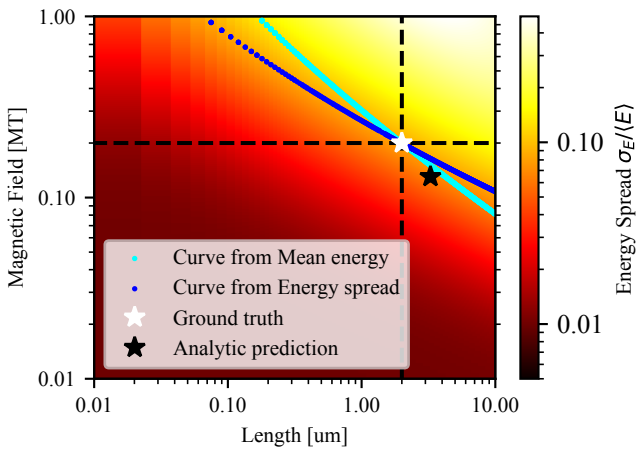

FIG. 5: Illustration of how we can use the mean energy and energy spread measurement of the electron beam before and after it passes through a constant magnetic field region to obtain the strength and the length of the field. The cyan curve and the blue curve represent all the potential magnetic field strength and length combinations for a particular mean energy and the energy spread. The crossing point of the two curves coincides with the ground truth from the PIC simulation, represented by a white star. The black star is the prediction using the analytic Eqns. (22) and (23).

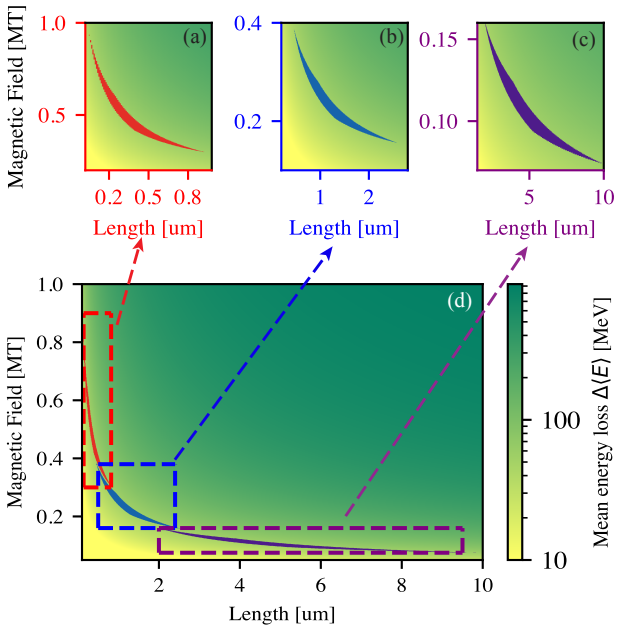

FIG. 6: Demonstration of the non-linear dependence of the aspect ratio of the overlapping region with the position of the region. Here we assume a 10% measurement error in mean energy loss and spread. For an energy loss of 51 MeV, the plot shows what the possible values of B-field strength and length are if the energy spread is 10%, 8%, or 6%, corresponding to the (a) red, (b) blue, and (c) purple areas in plot (d).

the methods outlined above have been demonstrated using LWFA from both target types, however novel targets with guiding channels from a capillary discharge[52] or an axicon lens focused into a long gas jet[67] may be implemented to achieve even higher energies (5-10 GeV).

At the exit of the gas jet or cell the electron beam will have a small spot size (μm) and divergence (mrad) and therefore can be used to probe the fields within a small region on the surface of the foil. The size of the beam when it reaches the foil is defined by the divergence and distance from the gas target to the foil where the fields are generated. To obtain an accurate measurement of the fields, the size of the beam should be smaller than the spatial variance of the target fields. For the mea-surement of the magnetic field strength this will require a beam with a size $\mathcal{O}(10\ \mu\text{m})$. This constrains the target to be placed a few mm to a cm from the gas target exit depending on the beam divergence angle. More complex measurements, for example detection of filaments from the Weibel instability[68], may require smaller beams.

As the electron beam exits the gas target, the laser will exit with it and can reflect from the foil target. If the foil target is placed normal to the electron beam propagation direction, the laser will reflected head-on into the electron beam and can scatter from the electron beam. Indeed, this is the experimental geometry proposed for multi-photon Compton scattering studies[69]. To avoid this, the quantum nonlinearity parameter η must be small, perhaps < 0.01 such that the rate of emission is low. To achieve this, the gas jet to target distance must be long enough to allow the laser to expand. The laser intensities used for LWFA are generally only mod-erately relativistic, with a normalized vector potential $a_0 = eE_L/m_e c\omega_L \sim 1-3$, where E_L is the laser electric field and ω_L is the laser frequency. Depending on the electron beam energy and separation, η may already be sufficiently small. However, if this condition is not met, potential solutions to this are to deflect the laser pulse using a thin foil placed between the gas jet and target, or to use beam optics to transport the electron beam far from the gas jet while maintaining the small beam size. There is limited space to place a reflecting foil between the gas target and main foil, therefore the main interac-tion laser may need to be incident on the back side of the foil i.e., the opposite side from what is shown in Fig. 7. Using a thin foil to reflect the laser away may also alter the electron beam properties by scattering in the foil or due to the fields generated on the foil surface. However, because the beam closely follows the laser pulse, there is limited time for fields to form on the foil. Addition-ally, these effects will also appear on the reference beam, i.e. the beam probing with the main interaction laser off, therefore the effects should already be accounted for by simply measuring the reference beam. Hot electrons will also propagate from the reflecting foil that will be

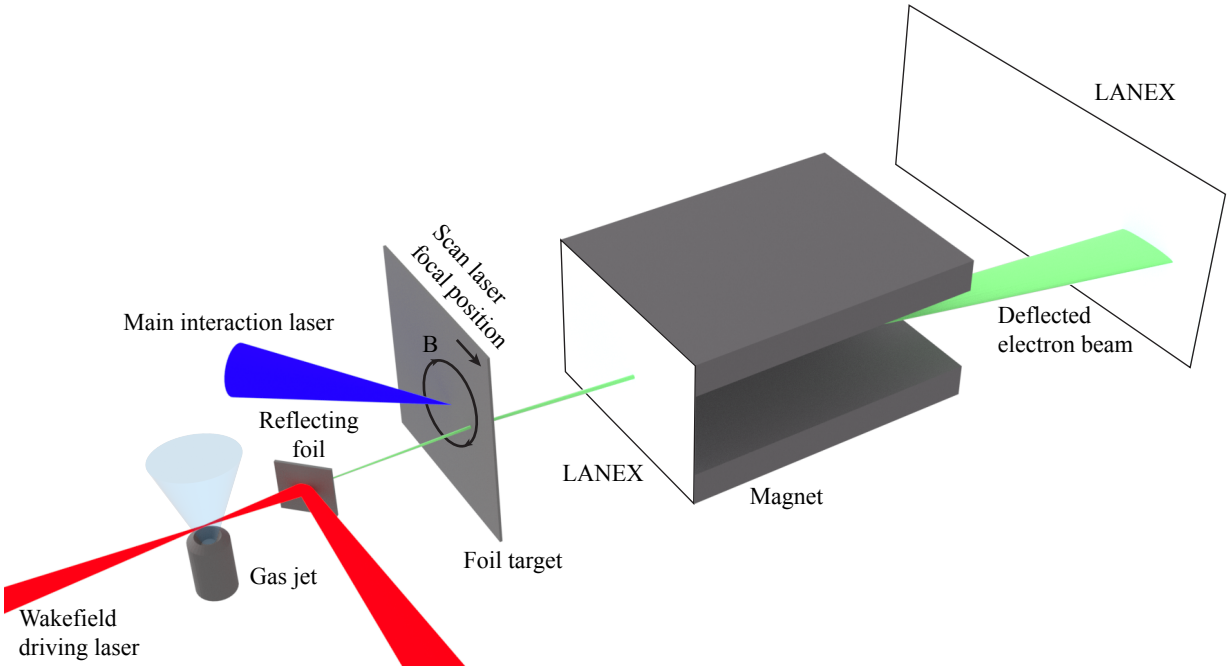

FIG. 7: Proposed experimental setup for the measurement of strong magnetic fields in laser-solid interactions.

incident on the target foil, however we expect the effect of these electrons on the fields of the target to be negli-gible because they should have a large divergence angle and much lower energies than the electrons accelerated on the main foil target.

As the beam propagates through the fields on the surface of the foil it will be deflected while simultaneously losing energy to radiation. To measure the change in energy, the beam that exits the foil will propagate to an electron spectrometer where it is dispersed onto a detector (LANEX). The LANEX is then imaged onto a CCD. Generally, to reduce the error of the electron spectrometer measurement an aperture should be placed before the magnet. However, the pointing of the beam into the magnet will vary depending on the fields that are probed on the target, making it difficult to position the aperture. Neglecting radiation reaction, this position will be described by Eqn. (15). As shown in Fig. 8, even with radiation reaction the position of the maximum is still well approximated by Eqn. (15). Therefore, based on the expected target magnetic fields, we can estimate the position of the beam. Additionally, if LANEX is placed before the dipole magnet and imaged onto a second CCD, the position and angle of the beam entering the dipole magnet field can be measured. The deflected position can be used to provide a measurement of the addition of the path integrated magnetic fields $B_{\perp,f} l_{B,f} + B_{\perp,b} l_{B,b}$ on the front and back surface of the target. To perform this measurement, the mean energy of the beam before deflection must be known. Therefore, a reference energy spectrum must be taken with the main interaction laser off. The spectrum can be measured from the beam that passes through the LANEX. For high energy electrons, scattering from the LANEX will be negligible.

Finally, note that the probe beam itself may affect the fields it is measuring. LWFA experiments demonstrat-ing multi-GeV electron beams have shown beam charges from approximately 1-100 pC[52]. Such beams are readily measured on LANEX, however with such high charge the fields induced in the target may modify the trajectory of the particles and therefore add error to the field measurement. To evaluate whether this effect is important, we can refer to the work of Sampath *et al.*[70]. As shown in their manuscript, a relativistic beam approaching a conducting surface will induce fields within the target that will act to focus the beam. Specifically, the azimuthal magnetic field of the beam will be amplified while the radial electric field will be reduced. Eqn. 1 from their manuscript can be used to evaluate the strength of the beam fields. For a 1 GeV, 10 pC beam with radial and parallel spreads of $\sigma_\perp = \sigma_\parallel = 1$ μm, the azimuthal magnetic field is ~ 108 T. This is approximately three orders of magnitude smaller than the fields being probed. We therefore expect this effect to have a negligible impact on the measurement.

B. Synthetic electron spectrometer

As shown in section III D, the energy spectrum of the beam will change due to radiation reaction, allowing for the calculation of $B^2_{\perp,f} l_{B,f} + B^2_{\perp,b} l_{B,b}$ and $B^3_{\perp,f} l_{B,f} + B^3_{\perp,b} l_{B,b}$. To determine whether this measurement is possible we propagated the beam output from the

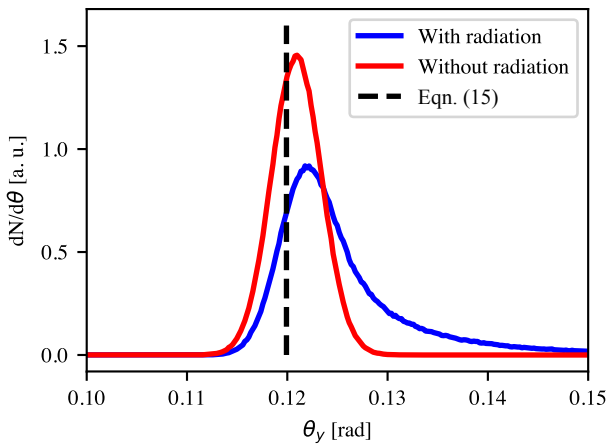

FIG. 8: Simulated deflection of a 1 GeV, 1% energy spread, 5 mrad divergence electron beam in 0.2 MT, 2 μm thick magnetic fields perpendicular to the propagation direction of the beam. The peak position of the deflection angle without radiation reaction is calculated using Eqn. (15), which is close to the peak position of the deflection angle with radiation reaction.

2D OSIRIS simulations through a custom particle tracking code specifically designed to model electron spectrometers. This code uses a Boris algorithm[71] particle pusher to calculate the particle trajectories through an analytic dipole field calculated from overlapping analytic fields from rectangular parallelepiped block magnets[72]. One percent of particles from the OSIRIS electron output population was sampled and sent through constant magnetic fields which are captured in the detector plane as shown in Fig. 9(a). The position of the electrons on the detector is related to their energy and divergence angle (Fig. 9(b)). In the detector plane, a 2D image of the dispersed electrons is formed where the transverse width of the line comes from the divergence of the beam and the length of the line is from the dispersion of electrons in the magnetic field (Fig. 9(c i) and (c ii)). The dispersion of these electrons greatly depends on the strength of the magnetic field and the geometry of the detector, i.e. length of magnets and position of LANEX. The error in the detection of the electron spectrum will depend on the dispersion error due to divergence of the beam, point-spread-function of the LANEX, and the imaging system used to collect the light from the LANEX. The choice of these components will result in an overall error in the measurement of the mean energy and energy spread of the electron beam.

C. Obtaining electron spectra

The most significant complication to measuring the electron spectra will come from electrons entering the magnetic fields of the electron spectrometer at different angles which will be the case for varying magnetic fields at the target. In order to obtain an energy spectrum from an electron beam that has been dispersed from a dipole magnetic field onto a scintillating screen, a mapping of energy to position on the screen is required, i.e. a dispersion curve of the electron spectrometer system. This dispersion curve not only depends on the geometry of the magnet(s) and screen(s), but also on the input beam's pointing angle into the system. It is therefore not only important to have LANEX before the dipole magnet to measure the deflection of the beam to calculate the path integrated fields, but also to construct the dispersion curve of the electron spectrometer. Once a pointing angle is measured, a dispersion curve for the resulting measurement may be simulated by tracking a range of particle energies through a particular electron spectrometer geometry using the measured pointing angle.

Fig. 9(b) shows the dispersion curves $E(x)$ generated by simulating the propagation of particles output from a 2D OSIRIS simulation through magnetic fields and onto two detectors. In the OSIRIS simulation a 1 GeV, 1% energy spread electron beam with a 5 mrad divergence was sent though a constant perpendicular 0.2 MT, 2 μm magnetic field. The unperturbed initial beam was propagated through the electron spectrometer code to generate the blue population of particles, and the beam after passing through the fields forms the red population. These populations enter the dipole magnet with a significant difference in pointing angle, therefore if both populations were dispersed onto the same LANEX screen, they would have different path lengths. This difference in path length would allow the blue population of electrons to expand more due to the divergence of the beam, increasing measurement error. From the histograms of electron energy as a function of relative screen position (Fig. 9(b)), particles with a range of energies are observed at the same screen position. This overlap of energies comes from the initial divergence of the electron beam. To reduce this error two LANEX screens can be used as shown in Fig. 9(a) and the position of the screens can be optimized to obtain well resolved spectra. Even after optimization there will be particles of different energies at the same screen position and the dispersion curve will then then be constructed by taking the average energy of electrons at a particular screen position, as was done to generate the dispersion curves in Fig. 9(b).

Using the simulated dispersion curve, $\langle E \rangle$ can be calculated and compared to the real value by taking an average of the raw electron data from OSIRIS. The average energies of the electrons sampled from our OSIRIS simulations are 999.5 MeV for the initial beam and 934.1 MeV for the beam that traversed the probed fields. By looking at the energy vs positions on the post-dipole LANEX screens, a dispersion curve can be fitted to the particle distributions. In our sampling, a 4th-order polynomial fit the initial beam average $E(x)$ distribution most closely, and a 5th-order polynomial best matched the average dispersion of the probed particles. These fitted disper-

sion relations interpolated to x-positions on the screens to give a measured energy distribution from the particle's longitudinal screen position. For our initial case, this resulted in a measured average energy of 987.3 MeV, and for the probed beam case this resulted in a measured average energy of 934.2 MeV. The measurement error comes from the divergence of the beam at the position of the screen and can likely be reduced through optimization of the screen positions. The average energy of the beam is greatly affected by low energy tail of particles that have experienced radiation reaction. In an experiment the measurement of these particles will be limited by the dynamic range of the detector and the background noise. This background will largely come from the main interaction foil where there will be a significant flux of electrons. These electrons will likely have much lower energies than the probing beam, however based on their large divergence angle and flux they may interact with the LANEX. Shielding may be necessary to reduce this background. Depending on the noise level, a significant part of this tail may be lost, adding error to the measurement of $\langle E \rangle$ and σ, thereby adding error to the calculation of B and l_B as was discussed in section III C.

An additional complication to the construction of an on-shot dispersion curve in an experiment is the energy dispersion that takes place in the beam due to the strong probed magnetic field causing particles of different energies to enter the dipole magnet with different pointing angles. By reading particles from OSIRIS simulations, this point was already taken into account in our dispersion curve, however this will not be possible with experimental data. In experiment, the pointing dependence of the energy spectra going into the magnetic spectrometer system can be measured using high-Z fiducial features, as has been done in previous experiments[73]. Coupled with a particle tracking code the dispersion curve can then be generated. Together, the fiducials and LANEX on the front of the magnet should also help account for shot-to-shot fluctuations in the beam pointing.

Although we have pointed out several complications with performing the proposed measurements, these are not unique problems of our measurement, but of generally diagnosing high-energy electron beams. We have only considered the most basic electron spectrometer setup, however as measurements of high energy beams become more prevalent, diagnostic techniques for measuring the properties of these beams should become more robust. Even with the spectrometer simulated here, taking into account the error due to beam divergence, the shift in mean energy is resolved.

V. CONCLUSIONS

Measuring the strong magnetic fields that are expected to be generated in the ultra-intense interactions of next-generation lasers facilities will be challenging. However, these measurements will be necessary if we plan to study magnetized processes at these facilities. The analysis techniques commonly used to obtain 2D maps of path integrated magnetic fields strength become invalid for field strengths well below the expected $\mathcal{O}(0.1$ MT) fields produced in laser-solid interactions. Novel measurement techniques including Faraday rotation of XFEL beams[10], electron spin[27], and deflectometry of LWFA electron beams as discusses here will be required. The most readily accessible method will be LWFA electron deflectometry as many of the ultra-intense facilities plan to already have energetic GeV beams and associated beam diagnostics for the proposed colliding beam experiments.

Compared to proton deflectometry, the use of LWFA electron beams will come with many additional complications that must be considered including the divergence angle, energy spread, and radiation reaction on the probe beam. As shown in this manuscript, energy spread and radiation reaction encode information on the strength and length of fields which can then be extracted. This is unlike standard deflectometry where only the path integrated fields can be measured. This lead us to propose an experimental setup where the laser-generated magnetic fields within a small region on a foil target are measured by a LWFA electron beam. The electron beam is sent through a scintillating screen before being dispersed through a dipole magnet onto a second scintillating screen. Such a setup allows for the measurement of the deflection angle of the electron beam after it probes the fields on the foil target which gives a measurement of the path integrated fields and is also necessary to obtain the dispersion curve for the dispersed electron beam to extract the energy spectrum. The laser interacting with the foil can then be rastered along the target to provide a measurement of the spatial variation of the fields. To measure a larger region of the fields on a single shot the beam may be focused to a line using beam optics placed before the target. However, accurately measuring the spectra of this beam will be challenging.

Measurement error and complications in the measurement were considered to a reasonable level of complexity. However, there will be additional, experiment specific complications depending on what fields are being probed and the particular experimental setup that is used. For example, one of the main complications of probing solid target fields is that the fields are generated on the front and back surfaces of the target. We considered this in a simplified way, however we neglected effects due to electric fields which may also be important, especially to the radiation reaction on the beam. The work presented here should therefore provide the framework for the setup of LWFA electrons as a probe, upon which any additional modifications can be made to account for experiment specific complications.

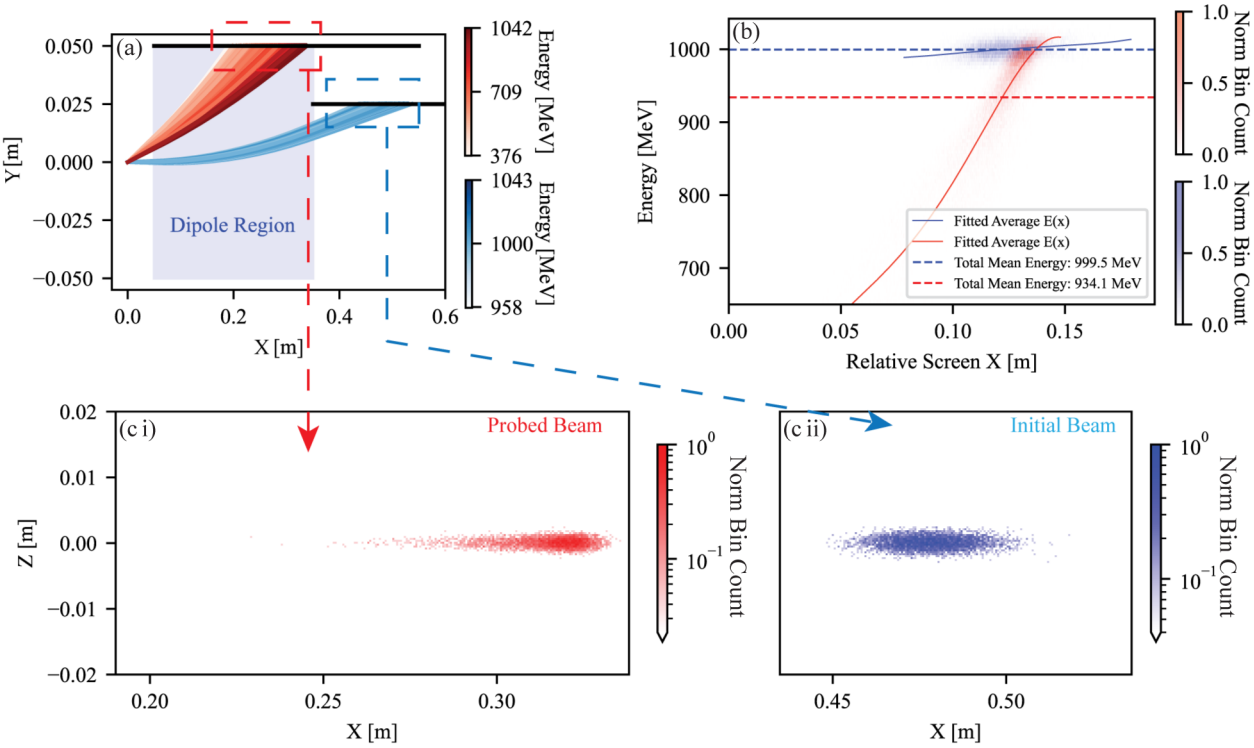

FIG. 9: (a) Electron trajectories through a 30 × 10 × 3 cm analytic dipole field region with a central magnetic field strength of 1 T placed 5 cm away from the probing point. An electron beam with an energy of 1 GeV with a 1% energy spread and 5 mrad divergence before (blue) and after (red) probing a 2 μm 0.2 MT field. (b) 2D histogram of electron energy vs relative longitudinal position on the respective screen. (c) Normalized bin counts assuming 200 μm × 200 μm pixels on the LANEX screens after the dipole for the beams with (c i) and without (c ii) the probed field.

ACKNOWLEDGEMENTS

This work was supported by the National Science Foundation under NSF award number 1751462. Additional support was provided by the NSF and Czech Science Foundation under NSF-GACR collaborative grant 2206059 and NSF grant 2108075. PTC was supported by the U.S. DOE Fusion Energy Sciences Postdoctoral Research Program administered by the Oak Ridge Institute for Science and Education (ORISE). ORISE is managed by Oak Ridge Associated Universities (ORAU) under DOE contract number DE-SC0014664. SSB was supported by U.S. Department of Energy Office of Science Offices of High Energy Physics and Fusion Energy Sciences (through LaserNetUS), under Contract No. DE-AC02-05CH11231. The authors acknowledge the OSIRIS Consortium, consisting of UCLA and IST (Portugal) for the use of the OSIRIS 4.0 framework.

AUTHOR DECLARATIONS

Conflict of Interest

The authors have no conflicts to disclose.

Author Contributions

Brandon K. Russell: conceptualization (equal); methodology (lead); visualization (equal); writing - original draft (lead). **Paul T. Campbell**: conceptualization (equal); formal analysis (supporting); visualization (equal); writing - original draft (supporting). **Qian Qian**: conceptualization (supporting); formal analysis (equal); methodology (supporting); software (supporting); visualization (equal); writing - original draft (supporting). **Jason A. Cardarelli**: conceptualization (supporting); formal analysis (equal); software (lead); visualization (equal); writing - original draft (supporting). **Stepan S. Bulanov**: writing - review and editing (equal). **Sergei V. Bulanov**: writing - review and editing (equal). **Gabriele M. Grittani**: writing - review and editing (equal). **Daniel Seipt**: writing - review and

editing (equal). **Louise Willingale**: conceptualization (supporting); funding acquisition (lead); writing - review and editing (equal). **Alexander G. R. Thomas**: conceptualization (equal); resources (lead); writing - review and editing (equal).

DATA AVAILABILITY

The data that support the findings of this study are available from the corresponding author upon reasonable request.

APPENDIX A: DERIVATION OF ENERGY SPREAD EQUATIONS

If we assume that the particle energies are not changing during the propagation of the beam through the fields, and the beam is propagating along the z-direction with magnetic field in the y-direction, then the deflections are given by,

$$\alpha_x(x_0, E) = \frac{ec}{E}\int_{-\infty}^{\infty} B_y(x_0)\, dz, \tag{A1}$$

which is derived from the ratio of v_x/v_z where $v_z \approx c$ and $E = \gamma mc^2$ is the energy of the particle which is approximately the kinetic energy for a highly relativistic particle. From Eqn. (A1) we can see that particles of different energies will be deflected to different angles with the highest energy particles seeing the smallest deflection. For the purpose of finding a resolution criteria based on energy spread we need to know the width of this angular spread in the image plane.

If the electrons have a Gaussian energy distribution and propagate to the object plane from a point source, they will have a distribution at the object plane of,

$$\frac{\partial^2 N}{\partial x_0 \partial E} \propto \exp\left(-\frac{(E-E_0)^2}{2\sigma_E^2}\right). \tag{A2}$$

At the object plane the electrons are deflected to a point in the image plane given by $x = x_0 + x_0 L/l + \alpha_x(x_0, E)L$. Rearranging this equation and substituting Eqn. (A1) for α_x gives,

$$E = \frac{ecL}{x - Mx_0}\mathcal{B}, \tag{A3}$$

where $\mathcal{B} = \int_{-\infty}^{\infty} B_y(x_0)\, dz$ and $M = (l+L)/l$ is the magnification. To find the distribution function in the image plane we multiply Eqn. (A2) by $\partial E/\partial x$ and substitute Eqn. (A3) for E. This gives the distribution function in the image plane,

$$\frac{\partial^2 N}{\partial x_0 \partial x} \propto \frac{-ecL\mathcal{B}}{(x-Mx_0)^2}\exp\left(-\frac{(\frac{ecL}{x-Mx_0}\mathcal{B} - E_0)^2}{2\sigma_E^2}\right). \tag{A4}$$

This equation is only valid for a relativistic beam where $v_z \approx c$ and therefore only valid for small $x - Mx_0$ where Eqn. (A3) is positive. A plot of this equation compared to results from a particle tracking code assuming deflections in a single plane is shown in Fig. 3. Particles are only deflected to one side of the position of a particle experiencing no deflection, i.e. $x = Mx_0$. If $\sigma_E \ll E_0$ then the maximum of this distribution occurs at the position,

$$x_{max} = \frac{ecL\mathcal{B}}{E_0} + Mx_0. \tag{A5}$$

The value of Eqn. (A4) at this position is given by,

$$\frac{\partial^2 N(x_{max})}{\partial x_0 \partial x} = -\frac{E_0^2}{ecL\mathcal{B}}, \tag{A6}$$

therefore Eqn. (A4) can be normalized by this value to give a maximum of 1. This maximum simply occurs at the peak position of the exponential because the shape of the beam spread in the image plane is dominated by the exponential term for small energy spreads. We can therefore take the full-width half-maximum (FWHM) of the exponential to define a resolution criterion based on energy spread. This FWHM is given by,

$$\Delta x_{energy} = ecL\mathcal{B}\frac{2\sqrt{2\ln(2)\sigma_E^2}}{E_0^2 - 2\ln(2)\sigma_E^2}. \tag{A7}$$

APPENDIX B: DERIVATION OF THE QUANTUM BROADENING EQUATION

The derivation of Eqn. (23) begins with Eqn. (18), rewritten here for convenience,

$$\left(\frac{d\sigma^2}{dt}\right)_{st} \approx \frac{\alpha_f c b^2}{\lambda\!\!\!^{-}_c}\left(\frac{55b}{24\sqrt{3}}\langle\gamma\rangle^4 - \frac{8}{3}\sigma^2\langle\gamma\rangle\right) \tag{B1}$$

First, replace $\langle\gamma\rangle$ using Eqn. (20) to give:

$$\xi^4\left(\frac{d\sigma^2}{dt}\right)_{st} + \xi^3\frac{8\alpha_f c b^2}{3\lambda\!\!\!^{-}_c}\sigma^2 - \frac{55\alpha_f c b^3}{24\sqrt{3}\lambda\!\!\!^{-}_c} = 0, \tag{B2}$$

where $\xi = \frac{1}{\langle\gamma_0\rangle} + \kappa t$. Since $\partial\xi/\partial t = \kappa$, we can change the derivative to:

$$\kappa\xi^4\left(\frac{d\sigma^2}{d\xi}\right)_{st} + \xi^3\frac{8\alpha_f c b^2}{3\lambda\!\!\!^{-}_c}\sigma^2 - \frac{55\alpha_f c b^3}{24\sqrt{3}\lambda\!\!\!^{-}_c} = 0. \tag{B3}$$

Next, rearrange the equation and let $G = \frac{55\alpha_f c b^3}{24\sqrt{3}\lambda\!\!\!^{-}_c}$:

$$\left(\frac{d\sigma^2}{d\xi}\right)_{st} + \frac{4}{\xi}\sigma^2 = \frac{G}{\kappa\xi^4}. \tag{B4}$$

This is a first-order inhomogeneous differential equation with variable coefficients. The solution to this equation can be found by first finding the solution to the homogeneous equation, i.e. set the right hand side equal to

zero and integrate. Additionally, use the initial condition, when $\xi = 1/\langle\gamma_0\rangle$, $\sigma^2 = \sigma_0^2$. The homogeneous solution is then:

$$\sigma_h^2 = \frac{\sigma_0^2}{(\langle\gamma_0\rangle\xi)^4} \tag{B5}$$

Next, find the particular solution by substituting the following equation for σ^2 in Eqn. (B4):

$$\sigma_p^2 = \frac{C(\xi)}{\xi^4} \tag{B6}$$

Additionally use the initial condition $C(1/\langle\gamma_0\rangle) = 0$. This results in the coefficient,

$$C(\xi) = \frac{G}{\kappa}\left(\xi - \frac{1}{\langle\gamma_0\rangle}\right). \tag{B7}$$

The sum of the homogeneous and particular solution when simplified, taking $b = cB_\perp/E_s$ results in Eqn. (23):

$$\sigma = \langle\gamma\rangle^2\sqrt{\frac{\sigma_0^2}{\langle\gamma_0\rangle^4} + At}, \tag{B8}$$

where $A = \alpha_f c^4 B_\perp^3 55/24E_s^3\sqrt{3}\lambda_c$.

REFERENCES

[1]C. N. Danson, C. Haefner, J. Bromage, T. Butcher, J.-C. F. Chanteloup, E. A. Chowdhury, A. Galvanauskas, L. A. Gizzi, H. J., D. I. Hillier, N. W. Hopps, Y. Kato, E. A. Khazanov, R. Kodama, K. G., R. Li, Y. Li, J. Limpert, J. Ma, C. H. Nam, D. Neely, D. Papadopoulos, R. R. Penman, L. Qian, J. J. Rocca, A. A. Shaykin, C. W. Siders, C. Spindloe, S. Szatmári, R. M. G. M. Trines, J. Zhu, Z. P., and J. D. Zuegel, "Petawatt and exawatt lasers worldwide," High Power Laser Science and Engineering **7**, e54 (2019).

[2]J. W. Yoon, Y. G. Kim, I. W. Choi, J. H. Sung, H. W. Lee, S. K. Lee, and C. H. Nam, "Realization of laser intensity over 10^{23}w/cm^2," Optica **8**, 630–635 (2021).

[3]J. Nees, A. Maksimchuk, G. Kalinchenko, B. Hou, Y. Ma, P. Campbell, A. McKelvey, L. Willingale, I. Jovanovic, C. Kuranz, A. Thomas, and K. Krushelnick, "Zeus: A national science foundation mid-scale facility for laser-driven science in the qed regime," in *2020 Conference on Lasers and Electro-Optics (CLEO)* (2020) pp. 1–2.

[4]A. D. Piazza, L. Willingale, and J. D. Zuegel, "Multi-petawatt physics prioritization (mp3) workshop report," (2022), arXiv:2211.13187 [hep-ph].

[5]A. Gonoskov, T. G. Blackburn, M. Marklund, and S. S. Bulanov, "Charged particle motion and radiation in strong electromagnetic fields," Rev. Mod. Phys. **94**, 045001 (2022).

[6]F. Albert and A. G. R. Thomas, "Applications of laser wakefield accelerator-based light sources," Plasma Physics and Controlled Fusion **58**, 103001 (2016).

[7]P. Zhang, S. S. Bulanov, D. Seipt, A. V. Arefiev, and A. G. R. Thomas, "Relativistic plasma physics in supercritical fields," Physics of Plasmas **27**, 050601 (2020).

[8]D. J. Stark, T. Toncian, and A. V. Arefiev, "Enhanced Multi-MeV Photon Emission by a Laser-Driven Electron Beam in a Self-Generated Magnetic Field," Physical Review Letters **116**, 185003 (2016).

[9]J. Park, S. S. Bulanov, J. Bin, Q. Ji, S. Steinke, J.-L. Vay, C. G. R. Geddes, C. B. Schroeder, W. P. Leemans, T. Schenkel, and E. Esarey, "Ion acceleration in laser generated megatesla magnetic vortex," Physics of Plasmas **26** (2019), 103108.

[10]T. Wang, T. Toncian, M. S. Wei, and A. V. Arefiev, "Structured targets for detection of megatesla-level magnetic fields through faraday rotation of xfel beams," Physics of Plasmas **26**, 013105 (2019).

[11]B. K. Russell, M. Vranic, P. T. Campbell, A. G. R. Thomas, K. M. Schoeffler, D. A. Uzdensky, and L. Willingale, "Magnetic field generation in laser-solid interactions at strong-field qed relevant intensities," , submitted.

[12]V. S. Berezinskii, S. V. Bulanov, V. L. Ginzburg, V. A. Dogel, and V. S. Ptuskin, *Astrophysics of cosmic rays.* (North Holland Publ. Co. Elsevier Sci. Publ. Amsterdam, 1990).

[13]D. A. Uzdensky, "Magnetic reconnection in extreme astrophysical environments," Space Sci. Rev. **160**, 45–71 (2022).

[14]S. V. Bulanov, "Magnetic reconnection: from mhd to qed," Plasma Physics and Controlled Fusion **59**, 014029 (2016).

[15]L. Sironi, U. Keshet, and M. Lemoine, "Relativistic shocks: Particle acceleration and magnetization," Space Science Reviews **191**, 519–544 (2015).

[16]M. C. Kaluza, H.-P. Schlenvoigt, S. P. D. Mangles, A. G. R. Thomas, A. E. Dangor, H. Schwoerer, W. B. Mori, Z. Najmudin, and K. M. Krushelnick, "Measurement of magnetic-field structures in a laser-wakefield accelerator," Phys. Rev. Lett. **105**, 115002 (2010).

[17]A. Buck, M. Nicolai, K. Schmid, C. M. S. Sears, A. Sävert, J. M. Mikhailova, F. Krausz, M. C. Kaluza, and L. Veisz, "Real-time observation of laser-driven electron acceleration," Nature Physics **7**, 543–548 (2011).

[18]M. Tatarakis, I. Watts, F. Beg, E. Clark, A. Dangor, A. Gopal, M. Haines, P. Norreys, U. Wagner, M.-S. Wei, M. Zepf, and K. Krushelnick, "Measuring huge magnetic fields," Nature **415**, 280–280 (2002).

[19]M. Borghesi, A. Schiavi, D. H. Campbell, M. G. Haines, O. Willi, A. J. MacKinnon, L. A. Gizzi, M. Galimberti, R. J. Clarke, and H. Ruhl, "Proton imaging: a diagnostic for inertial confinement fusion/fast ignitor studies," Plasma Physics and Controlled Fusion **43**, A267 (2001).

[20]W. Schumaker, N. Nakanii, C. McGuffey, C. Zulick, V. Chyvkov, F. Dollar, H. Habara, G. Kalintchenko, A. Maksimchuk, K. A. Tanaka, A. G. R. Thomas, V. Yanovsky, and K. Krushelnick, "Ultrafast electron radiography of magnetic fields in high-intensity laser-solid interactions," Physical Review Letters **110**, 015003 (2013).

[21]C. J. Zhang, J. F. Hua, Y. Wan, C.-H. Pai, B. Guo, J. Zhang, Y. Ma, F. Li, Y. P. Wu, H.-H. Chu, Y. Q. Gu, X. L. Xu, W. B. Mori, C. Joshi, J. Wang, and W. Lu, "Femtosecond probing of plasma wakefields and observation of the plasma wake reversal using a relativistic electron bunch," Physical Review Letters **119**, 064801 (2017).

[22]Y. Wan, S. Tata, O. Seemann, E. Y. Levine, S. Smartsev, E. Kroupp, and V. Malka, "Femtosecond electron microscopy of relativistic electron bunches," Light: Science & Applications **12**, 116 (2023).

[23]Y. Wan, O. Seemann, S. Tata, I. A. Andriyash, S. Smartsev, E. Kroupp, and V. Malka, "Direct observation of relativistic broken plasma waves," Nature Physics **18**, 1186–1190 (2022).

[24]G. Bruhaug, M. S. Freeman, H. G. Rinderknecht, L. P. Neukirch, C. H. Wilde, F. E. Merrill, J. R. Rygg, M. S. Wei, G. W. Collins, and J. L. Shaw, "Single-shot electron radiography using a laser–plasma accelerator," Scientific Reports **13**, 2227 (2023).

[25]C. Zhang, J. Hua, Y. Wu, Y. Fang, Y. Ma, T. Zhang, S. Liu, B. Peng, Y. He, C.-K. Huang, K. A. Marsh, W. B. Mori, W. Lu, and C. Joshi, "Measurements of the growth and saturation of electron weibel instability in optical-field ionized plasmas," Phys. Rev. Lett. **125**, 255001 (2020).

[26]C. Zhang, Y. Wu, M. Sinclair, A. Farrell, K. A. Marsh, I. Petrushina, N. Vafaei-Najafabadi, A. Gaikwad, R. Kupfer,

K. Kusche, M. Fedurin, I. Pogorelsky, M. Polyanskiy, C.-K. Huang, J. Hua, W. Lu, W. B. Mori, and C. Joshi, "Mapping the self-generated magnetic fields due to thermal weibel instability," Proceedings of the National Academy of Sciences **119**, e2211713119 (2022).

[27]Z. Gong, K. Z. Hatsagortsyan, and C. H. Keitel, "Retrieving transient magnetic fields of ultrarelativistic laser plasma via ejected electron polarization," Phys. Rev. Lett. **127**, 165002 (2021).

[28]P. M. Nilson, L. Willingale, M. C. Kaluza, C. Kamperidis, S. Minardi, M. S. Wei, P. Fernandes, M. Notley, S. Bandyopadhyay, M. Sherlock, R. J. Kingham, M. Tatarakis, Z. Najmudin, W. Rozmus, R. G. Evans, M. G. Haines, A. E. Dangor, and K. Krushelnick, "Magnetic reconnection and plasma dynamics in two-beam laser-solid interactions," Physical Review Letters **97**, 255001 (2006).

[29]Y.-J. Gu and S. V. Bulanov, "Magnetic field annihilation and charged particle acceleration in ultra-relativistic laser plasmas," High Power Laser Science and Engineering **9**, e2 (2021).

[30]D. B. Schaeffer, A. F. A. Bott, M. Borghesi, K. A. Flippo, W. Fox, J. Fuchs, C. Li, H.-S. Park, F. H. Seguin, P. Tzeferacos, and L. Willingale, "Proton imaging of high-energy-density laboratory plasmas," (2022), arXiv:2212.08252 [physics.plasm-ph].

[31]L. Gao, P. M. Nilson, I. V. Igumenshchev, M. G. Haines, D. H. Froula, R. Betti, and D. D. Meyerhofer, "Precision mapping of laser-driven magnetic fields and their evolution in high-energy-density plasmas," Physical Review Letters **114**, 215003 (2015).

[32]P. T. Campbell, C. A. Walsh, B. K. Russell, J. P. Chittenden, A. Crilly, G. Fiksel, P. M. Nilson, A. G. R. Thomas, K. Krushelnick, and L. Willingale, "Magnetic signatures of radiation-driven double ablation fronts," Phys. Rev. Lett. **125**, 145001 (2020).

[33]P. T. Campbell, C. A. Walsh, B. K. Russell, J. P. Chittenden, A. Crilly, G. Fiksel, L. Gao, I. V. Igumenshchev, P. M. Nilson, A. G. R. Thomas, K. Krushelnick, and L. Willingale, "Measuring magnetic flux suppression in high-power laser–plasma interactions," Phys. Plasmas **29**, 012701 (2022).

[34]G. Sarri, A. Macchi, C. A. Cecchetti, S. Kar, T. V. Liseykina, X. H. Yang, M. E. Dieckmann, J. Fuchs, M. Galimberti, L. A. Gizzi, R. Jung, I. Kourakis, J. Osterholz, F. Pegoraro, A. P. L. Robinson, L. Romagnani, O. Willi, and M. Borghesi, "Dynamics of self-generated, large amplitude magnetic fields following high-intensity laser matter interaction," Physical Review Letters **109**, 205002 (2012).

[35]W. Fox, G. Fiksel, A. Bhattacharjee, P.-Y. Chang, K. Germaschewski, S. X. Hu, and P. M. Nilson, "Filamentation instability of counterstreaming laser-driven plasmas," Physical Review Letters **111**, 225002 (2013).

[36]N. L. Kugland, D. D. Ryutov, P.-Y. Chang, R. P. Drake, G. Fiksel, D. H. Froula, S. H. Glenzer, G. Gregori, M. Grosskopf, M. Koenig, Y. Kuramitsu, C. Kuranz, M. C. Levy, E. Liang, J. Meinecke, F. Miniati, T. Morita, A. Pelka, C. Plechaty, R. Presura, A. Ravasio, B. A. Remington, B. Reville, J. S. Ross, Y. Sakawa, A. Spitkovsky, H. Takabe, and H.-S. Park, "Self-organized electromagnetic field structures in laser-produced counter-streaming plasma," Nature Physics **8**, 809–812 (2012).

[37]L. Willingale, P. M. Nilson, A. G. R. Thomas, J. Cobble, R. S. Craxton, A. Maksimchuck, P. A. Norreys, T. C. Sangster, R. H. H. Scott, C. Stoeckl, C. Zulick, and K. Krushelnick, "High-power, kilojoule class laser channeling in millimeter-scale underdense plasma," Physical Review Letters **106** (2011).

[38]C. K. Li, F. H. Séguin, J. A. Frenje, J. R. Rygg, R. D. Petrasso, R. P. J. Town, O. L. Landen, J. P. Knauer, and V. A. Smalyuk, "Observation of megagauss-field topology changes due to magnetic reconnection in laser-produced plasmas," Physical Review Letters **99**, 055001 (2007).

[39]L. Willingale, P. M. Nilson, M. C. Kaluza, A. E. Dangor, R. G. Evans, P. Fernandes, M. G. Haines, C. Kamperidis, R. J. Kingham, C. P. Ridgers, M. Sherlock, A. G. R. Thomas, M. S. Wei, Z. Najmudin, K. Krushelnick, S. Bandyopadhyay, M. Notley, S. Minardi, M. Tatarakis, and W. Rozmus, "Proton deflectometry of a magnetic reconnection geometry," Physics of Plasmas **17**, 043104 (2010).

[40]G. Fiksel, W. Fox, A. Bhattacharjee, D. H. Barnak, P. Y. Chang, K. Germaschewski, S. X. Hu, and P. M. Nilson, "Magnetic reconnection between colliding magnetized laser-produced plasma plumes," Physical Review Letters **113**, 105003 (2014).

[41]C. A. J. Palmer, P. T. Campbell, Y. Ma, L. Antonelli, A. F. A. Bott, G. Gregori, J. Halliday, Y. Katzir, P. Kordell, K. Krushelnick, S. V. Lebedev, E. Montgomery, M. Notley, D. C. Carroll, C. P. Ridgers, A. A. Schekochihin, M. J. V. Streeter, A. G. R. Thomas, E. R. Tubman, N. Woolsey, and L. Willingale, "Field reconstruction from proton radiography of intense laser driven magnetic reconnection," Physics of Plasmas **26**, 083109 (2019).

[42]S. P. Hatchett, C. G. Brown, T. E. Cowan, E. A. Henry, J. S. Johnson, M. H. Key, J. A. Koch, A. B. Langdon, B. F. Lasinski, R. W. Lee, A. J. Mackinnon, D. M. Pennington, M. D. Perry, T. W. Phillips, M. Roth, T. C. Sangster, M. S. Singh, R. A. Snavely, M. A. Stoyer, S. C. Wilks, and K. Yasuike, "Electron, photon and ion beams from the relativisit interaction of petawatt laser pulses with solid targets," Physics of Plasmas **7** (2000).

[43]A. Maksimchuk, S. Gu, K. Flippo, D. Umstadter, and V. Y. Bychenkov, "Forward ion acceleration in thin films driven by a high-intensity laser," Physical Review Letters **84** (2000).

[44]R. A. Snavely, M. H. Key, S. P. Hatchett, T. E. Cowan, M. Roth, T. W. Phillips, M. A. Stoyer, E. A. Henry, T. C. Sangster, M. S. Singh, S. C. Wilks, A. MacKinnon, A. Offenberger, D. M. Pennington, K. Yasuike, A. B. Langdon, B. F. Lasinski, J. Johnson, M. D. Perry, and E. M. Campbell, "Intense high-energy proton beams from petawatt-laser irradiation of solids," Physical Review Letters **85**, 2945 (2000).

[45]E. L. Clark, K. Krushelnick, J. R. Davies, M. Zepf, F. N. Beg, M. Tatarikis, A. Machacek, P. A. Norreys, M. I. K. Santala, I. Watts, and A. E. Dangor, "Measurment of energetic proton transport through magnetized plasma from intense laser interactions with solids," Physical Review Letters **84**, 670 (2000).

[46]F. Wagner, O. Deppert, C. Brabetz, P. Fiala, A. Kleinschmidt, P. Poth, V. A. Schanz, A. Tebartz, B. Zielbauer, M. Roth, T. Stöhlker, and V. Bagnoud, "Maximum Proton Energy above 85 MeV from the Relativistic Interaction of Laser Pulses with Micrometer Thick CH2 Targets," Physical Review Letters **116**, 205002 (2016).

[47]S. Keppler, N. Elkina, G. A. Becker, J. Hein, M. Hornung, M. Mäusezahl, C. Rödel, I. Tamer, M. Zepf, and M. C. Kaluza, "Intensity scaling limitations of laser-driven proton acceleration in the tnsa-regime," Phys. Rev. Res. **4**, 013065 (2022).

[48]M. Borghesi, D. H. Campbell, A. Schiavi, M. G. Haines, O. Willi, A. J. MacKinnon, P. Patel, L. A. Gizzi, M. Galimberti, R. J. Clarke, F. Pegoraro, H. Ruhl, and S. Bulanov, "Electric field detection in laser-plasma interaction experiments via the proton imaging technique," Physics of Plasmas **9**, 2214–2220 (2002).

[49]N. L. Kugland, D. D. Ryutov, C. Plechaty, J. S. Ross, and H.-S. Park, "Invited article: Relation between electric and magnetic field structures and their proton-beam images," Review of Scientific Instruments **83**, 101301 (2012).

[50]M. F. Kasim, L. Ceurvorst, N. Ratan, J. Sadler, N. Chen, A. Sävert, R. Trines, R. Bingham, P. N. Burrows, M. C. Kaluza, and P. Norreys, "Quantitative shadowgraphy and proton radiography for large intensity modulations," Physical Review E **95**, 023306 (2017).

[51]A. F. A. Bott, C. Graziani, P. Tzeferacos, T. G. White, D. Q. Lamb, G. Gregori, and A. A. Schekochihin, "Proton imaging of stochastic magnetic fields," Journal of Plasma Physics **83**, 905830614 (2017).

[52]A. J. Gonsalves, K. Nakamura, J. Daniels, C. Benedetti, C. Pieronek, T. C. H. de Raadt, S. Steinke, J. H. Bin, S. S. Bulanov, J. van Tilborg, C. G. R. Geddes, C. B. Schroeder, C. Tóth, E. Esarey, K. Swanson, L. Fan-Chiang, G. Bagdasarov, N. Bobrova, V. Gasilov, G. Korn, P. Sasorov, and W. P. Leemans, "Petawatt laser guiding and electron beam acceleration to 8 gev in a laser-heated capillary discharge waveguide," Phys. Rev. Lett.

122, 084801 (2019).
[53]A. Higginson, R. J. Gray, M. King, R. J. Dance, S. D. R. Williamson, N. M. H. Butler, R. Wilson, R. Capdessus, C. Armstrong, J. S. Green, S. J. Hawkes, P. Martin, W. Q. Wei, S. R. Mirfayzi, X. H. Yuan, S. Kar, M. Borghesi, R. J. Clarke, D. Neely, and P. McKenna, "Near-100 mev protons via a laser-driven transparency-enhanced hybrid acceleration scheme," Nature Communications **9**, 724 (2018).
[54]T. Ziegler, I. Gothel, S. Assenbaum, C. Bernert, F.-E. Brack, T. E. Cowan, N. P. Dover, L. Gaus, T. Kluge, S. Kraft, F. Kroll, J. Metzkes-Ng, M. Nishiuchi, I. Prencipe, T. Püschel, M. Rehwald, M. Reimold, and H.-P. Schlenvoigt, "Laser-driven high-energy proton beams from cascaded acceleration regimes," , submitted.
[55]S. S. Bulanov, V. Y. Bychenkov, V. Chvykov, G. Kalinchenko, D. W. Litzenberg, T. Matsuoka, A. G. R. Thomas, L. Willingale, V. Yanovsky, K. Krushelnick, and A. Maksimchuk, "Generation of GeV protons from 1 PW laser interaction with near critical density targets," Physics of Plasmas **17**, 043105 (2010).
[56]S. Bulanov and V. Khoroshkov, "Feasibility of using laser ion accelerators in proton therapy." Plasma Physics Reports **28**, 453–456 (2002).
[57]T. Z. Esirkepov, S. V. Bulanov, K. Nishihara, T. Tajima, F. Pegoraro, V. S. Khoroshkov, K. Mima, H. Daido, Y. Kato, Y. Kitagawa, K. Nagai, and S. Sakabe, "Proposed double-layer target for the generation of high-quality laser-accelerated ion beams," Phys. Rev. Lett. **89**, 175003 (2002).
[58]S. V. Bulanov, J. J. Wilkens, T. Z. Esirkepov, G. Korn, G. Kraft, S. D. Kraft, M. Molls, and V. S. Khoroshkov, "Laser ion acceleration for hadron therapy," Physics-Uspekhi **57**, 1149 (2014).
[59]Z. Zhou, Y. Fang, H. Chen, Y. Wu, Y. Du, L. Yan, C. Tang, and W. Huang, "Demonstration of single-shot high-quality cascaded high-energy-electron radiography using compact imaging lenses based on permanent-magnet quadrupoles," Phys. Rev. Appl. **11**, 034068 (2019).
[60]H. Wiedemann, *Particle accelerator physics* (Springer Nature, 2015).
[61]J. van Tilborg, S. Steinke, C. G. R. Geddes, N. H. Matlis, B. H. Shaw, A. J. Gonsalves, J. V. Huijts, K. Nakamura, J. Daniels, C. B. Schroeder, C. Benedetti, E. Esarey, S. S. Bulanov, N. A. Bobrova, P. V. Sasorov, and W. P. Leemans, "Active plasma lensing for relativistic laser-plasma-accelerated electron beams," Phys. Rev. Lett. **115**, 184802 (2015).
[62]K. Nakamura, A. J. Gonsalves, C. Lin, A. Smith, D. Rodgers, R. Donahue, W. Byrne, and W. P. Leemans, "Electron beam charge diagnostics for laser plasma accelerators," Phys. Rev. ST Accel. Beams **14**, 062801 (2011).
[63]C. Ridgers, T. Blackburn, D. Del Sorbo, L. Bradley, C. Slade-Lowther, C. Baird, S. Mangles, P. McKenna, M. Marklund, C. Murphy, *et al.*, "Signatures of quantum effects on radiation reaction in laser–electron-beam collisions," Journal of Plasma Physics **83** (2017).
[64]R. A. Fonseca, L. O. Silva, F. S. Tsung, V. K. Decyk, W. Lu, C. Ren, W. B. Mori, S. Deng, S. Lee, T. Katsouleas, and J. C. Adam, "Osiris: A three-dimensional, fully relativistic particle in cell code for modeling plasma based accelerators," in *Computational Science — ICCS 2002*, edited by P. M. A. Sloot, A. G. Hoekstra, C. J. K. Tan, and J. J. Dongarra (Springer Berlin Heidelberg, Berlin, Heidelberg, 2002) pp. 342–351.
[65]R. G. Hemker, "Particle-in-cell modeling of plasma-based accelerators in two and three dimensions," arXiv preprint arXiv:1503.00276 (2015).
[66]A. E. Raymond, C. F. Dong, A. McKelvey, C. Zulick, N. Alexander, A. Bhattacharjee, P. T. Campbell, H. Chen, V. Chvykov, E. Del Rio, P. Fitzsimmons, W. Fox, B. Hou, A. Maksimchuk, C. Mileham, J. Nees, P. M. Nilson, C. Stoeckl, A. G. R. Thomas, M. S. Wei, V. Yanovsky, K. Krushelnick, and L. Willingale, "Relativistic-electron-driven magnetic reconnection in the laboratory," Physical Review E **98**, 043207 (2018).
[67]B. Miao, J. E. Shrock, L. Feder, R. C. Hollinger, J. Morrison, R. Nedbailo, A. Picksley, H. Song, S. Wang, J. J. Rocca, and H. M. Milchberg, "Multi-gev electron bunches from an all-optical laser wakefield accelerator," Phys. Rev. X **12**, 031038 (2022).
[68]N. Shukla, K. Schoeffler, E. Boella, J. Vieira, R. Fonseca, and L. O. Silva, "Interplay between the weibel instability and the biermann battery in realistic laser-solid interactions," Phys. Rev. Research **2**, 023129 (2020).
[69]K. Ta Phuoc, S. Corde, C. Thaury, V. Malka, A. Tafzi, J. P. Goddet, R. C. Shah, S. Sebban, and A. Rousse, "All-optical compton gamma-ray source," Nature Photonics **6**, 308–311 (2012).
[70]A. Sampath, X. Davoine, S. Corde, L. Gremillet, M. Gilljohann, M. Sangal, C. H. Keitel, R. Ariniello, J. Cary, H. Ekerfelt, C. Emma, F. Fiuza, H. Fujii, M. Hogan, C. Joshi, A. Knetsch, O. Kononenko, V. Lee, M. Litos, K. Marsh, Z. Nie, B. O'Shea, J. R. Peterson, P. S. M. Claveria, D. Storey, Y. Wu, X. Xu, C. Zhang, and M. Tamburini, "Extremely dense gamma-ray pulses in electron beam-multifoil collisions," Phys. Rev. Lett. **126**, 064801 (2021).
[71]*Relativistic plasma simulation–optimization of a hybrid code, Proceedings: Fourth Conference on Numerical Simulation of Plasmas* (Naval Research Laboratory, Washington D.C., 1970).
[72]J. Lindl, "Potential and force between a magnet and a bulk y1ba2cu3o7- superconductor studied by a mechanical pendulum," Superconductor Science and Technology **3**, 591–597 (1990).
[73]C. E. Clayton, J. E. Ralph, F. Albert, R. A. Fonseca, S. H. Glenzer, C. Joshi, W. Lu, K. A. Marsh, S. F. Martins, W. B. Mori, A. Pak, F. S. Tsung, B. B. Pollock, J. S. Ross, L. O. Silva, and D. H. Froula, "Self-guided laser wakefield acceleration beyond 1 gev using ionization-induced injection," Phys. Rev. Lett. **105**, 105003 (2010).